UILU-ENG-91-2001

CIVIL ENGINEERING STUDIES

STRUCTURAL RESEARCH SERIES NO. 558

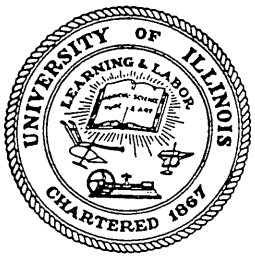

ISSN: 0069-4274

A LARGE STRAIN PLASTICITY MODEL FOR IMPLICIT FINITE ELEMENT ANALYSES

By
ROBERT H. DODDS, JR.
and
BRIAN E. HEALY

A Report on a Research Project
Sponsored by the
DAVID TAYLOR RESEARCH CENTER
METALS AND WELDING DIVISION
ANNAPOLIS, MARYLAND
Research Contract: N61533-88-C-0035

DEPARTMENT OF CIVIL ENGINEERING
UNIVERSITY OF ILLINOIS AT
URBANA-CHAMPAIGN
URBANA, ILLINOIS
JANUARY 1991

50272-101

REPORT DOCUMENTATION PAGE	1. REPORT NO. UILU-ENG-91-2001	2.	3. Recipient's Accession No.

4. Title and Subtitle
A Large Strain Plasticity Model for Implicit Finite Element Analyses

5. Report Date
January 1991

6.

7. Author(s)
R.H. Dodds, Jr. and B.E. Healy

8. Performing Organization Report No.
SRS 558

9. Performing Organization Name and Address
University of Illinois at Urbana-Champaign
Department of Civil Engineering
205 N. Mathews Avenue
Urbana, Illinois 61801

10. Project/Task/Work Unit No.

11. Contract(C) or Grant(G) No.
N61533-88-C-0035

12. Sponsoring Organization Name and Address
David Taylor Research Center
Metal and Welding Division, Code 281
Annapolis, Maryland 21542

13. Type of Report & Period Covered
Annual:11-1-89 to 12-31-90

14.

15. Supplementary Notes

16. Abstract (Limit: 200 words)

The theoretical basis and numerical implementation of a plasticity model suitable for finite strains and rotations are described. The constitutive equations governing J_2 flow theory are formulated using strains-stresses and their rates defined on the *unrotated* frame of reference. Unlike models based on the classical Jaumann (or corotational) stress rate, the present model predicts physically acceptable responses for homogeneous deformations of exceedingly large magnitude. The associated numerical algorithms accommodate the large strain increments that arise in finite-element formulations employing an implicit solution of the global equilibrium equations. The resulting computational framework divorces the finite rotation effects on strain-stress rates from integration of the rates to update the material response over a load (time) step. Consequently, all of the numerical refinements developed previously for small-strain plasticity (radial return with subincrementation, plane stress modifications, kinematic hardening, consistent tangent operators) are utilized without modification. Details of the numerical algorithms are provided including the necessary transformation matrices and additional techniques required for finite deformations in plane stress. Several numerical examples are presented to illustrate the realistic responses predicted by the model and the robustness of the numerical procedures.

17. Document Analysis a. Descriptors

Large Strains, Large Rotations, Plasticity, Finite Elements, Numerical Methods, Implicit, Total Lagrangian

b. Identifiers/Open-Ended Terms

c. COSATI Field/Group

18. Availability Statement	19. Security Class (This Report)	21. No. of Pages
Release Unlimited	UNCLASSIFIED	34
	20. Security Class (This Page) UNCLASSIFIED	22. Price

(See ANSI-Z39.18)

OPTIONAL FORM 272 (4-77)
Department of Commerce

A LARGE STRAIN PLASTICITY MODEL FOR IMPLICIT FINITE ELEMENT ANALYSES

By

Robert H. Dodds, Jr.

and

Brian E. Healy

Department of Civil Engineering
University of Illinois

A Report on a Research Project Sponsored by the:

DAVID TAYLOR RESEARCH CENTER
METALS AND WELDING DIVISION

Annapolis, Maryland 21402

University of Illinois
Urbana, Illinois
January 1991

ABSTRACT

The theoretical basis and numerical implementation of a plasticity model suitable for finite strains and rotations are described. The constitutive equations governing J_2 flow theory are formulated using strains–stresses and their rates defined on the *unrotated* frame of reference. Unlike models based on the classical Jaumann (or corotational) stress rate, the present model predicts physically acceptable responses for homogeneous deformations of exceedingly large magnitude. The associated numerical algorithms accommodate the large strain increments that arise in finite–element formulations employing an implicit solution of the global equilibrium equations. The resulting computational framework divorces the finite rotation effects on strain–stress rates from integration of the rates to update the material response over a load (time) step. Consequently, all of the numerical refinements developed previously for small–strain plasticity (radial return with subincrementation, plane stress modifications, kinematic hardening, consistent tangent operators) are utilized without modification. Details of the numerical algorithms are provided including the necessary transformation matrices and additional techniques required for finite deformations in plane stress. Several numerical examples are presented to illustrate the realistic responses predicted by the model and the robustness of the numerical procedures.

ACKNOWLEDGMENTS

The first author (R.H. Dodds) was supported by the David Taylor Research Center Metals and Welding Division (Code 281), Annapolis, Maryland under contract N61533–88–C–0035 to the University of Illinois. The second author (B.E. Healy) acknowledges support provided by the Center for Supercomputing Research and Development under grant SCCA 90–82144 from the Illinois Dept. of Commerce. Computations reported here were performed on an Apollo DN–10000 workstation operated by the Department of Civil Engineering. Acquisition of this computer was made possible by a grant from Hewlett–Packard, Inc.

TABLE OF CONTENTS

LIST OF TABLES

LIST OF FIGURES

A LARGE STRAIN PLASTICITY MODEL FOR IMPLICIT FINITE ELEMENT ANALYSES

1. INTRODUCTION

High–end workstations and mini–supercomputers are making feasible the routine consideration of plasticity with large strain and rotation effects in finite–element analyses. Such diverse phenomenon as post–buckling deformations, metal forming, contact/indentation and the micromechanics of ductile fracture may be realistically modeled. Finite rotations of material axes (those attached to material points that rotate with the continuum in a local sense) complicate the definition of strain–stress rates and their numerical integration to advance the material response over a load (or time) step. Traditionally, constitutive models for large strain plasticity in finite–element codes are cast in a spatial setting which mandates use of an *objective* stress rate to remove that part of the total stress rate due to simple rigid rotation of the material. In a spatial setting, the components of Cauchy (true) stress are defined relative to a fixed, Cartesian system; thus rigid rotation alone alters the stress components. While numerous objective stress rates may be constructed [2] with each leading to a potentially different material response, the Jaumann stress rate has been implemented universally in both explicit and implicit codes given its apparent simplicity, for example [17] and [1].

Over the past ten years, serious objections to constitutive models employing the Jaumann rate have developed as more complex material behavior is considered (e.g., kinematic hardening and viscoplasticity) and as the magnitude of deformations experienced in the applications has increased (plastic strains exceeding 50–100%). The first objection addresses the increased complexity of numerical algorithms to accommodate the spatial setting; tensorial state variables within the plasticity model, for example, the back–stress in kinematic hardening, must also be expressed using an objective rate and modified to reflect finite rotations. Processing of the purely kinematic effects due to finite rotations is thus interwoven with integration of evolution equations for the internal state variables. Consequently, development of each new material model requires potentially individual treatment of finite rotations. The second objection to use of the Jaumann rate concerns the physically unacceptable stresses predicted at large strains under certain conditions. The problem of simple finite shear illustrates the deficiency [5]. An incremental, linear–elastic material law is used to relate the Jaumann stress rate to the rate of deformation expressed in a fixed Cartesian system. The predicted Cauchy stresses oscillate in an unrealistic manner (σ_{12} actually reverses sign) . Nagtegaal and de Jong [22] noted such stress

oscillations with kinematic hardening in elasto–plasticity for a material which strain hardens monotonically in tension. Atluri [2] later showed that similar oscillations exist for isotropic hardening unless the elastic strains are vanishingly small. The oscillatory response derives from the constant spin *rate* tensor characteristic of simple shear while the actual rigid–body rotation diminishes with increasing deformation, approaching $\pi/2$ in the limit. The Cauchy stress obtained using the constant spin tensor becomes erroneous once the logarithmic shear strain, γ_{12}, exceeds 100%.

Atluri [2] demonstrated that removal of the oscillatory response in simple shear may be accomplished through definition of alternate stress rates or through a more general construction of the hypo–elastic material law. In a desire to retain the simplest hypo–elastic material law as a direct generalization of the conventional small–strain forms, Green and Naghdi [9] introduced an objective stress rate that has been discussed extensively by Dienes [5], Johnson and Bammann [15] and Atluri [2]. A Cauchy stress measure and its objective rate are defined on an *unrotated* orthogonal reference frame established through polar decomposition of the total deformation gradient at each material point. This constitutive model predicts monotonically increasing stresses in simple shear for incremental, linear–elasticity. Using this concept of an unrotated reference frame for constitutive modeling, Flanagan and Taylor [8] developed the PRONTO 2–D and 3–D [32] codes for transient dynamic analysis with explicit time integration. An impressive collection of material behaviors and contact algorithms are included in these codes. Constitutive computations are performed using strains, stresses and their objective rates defined on the unrotated reference frame. Effects of finite rotations are thus transparent to integration algorithms for stresses and the material state variables. The numerical architecture of existing small–strain plasticity models is fully retained. Flanagan and Taylor note their computational challenge was development of an exceptionally efficient algorithm for evolution of the polar decomposition with time in the globally explicit solution.

The present paper describes the implementation and performance of the unrotated reference frame concept for finite–element solutions that use implicit methods to resolve the global equilibrium equations and as such represents an extension of Flanagan and Taylor's work. While efficient methods for polar decomposition remain an issue, two additional challenges face the developer of an implicit code: 1) efficient and accurate schemes to integrate the plasticity rate equations over the very large strain increments characteristic of implicit methods, and 2) consistent tangent operators to maintain quadratic rates of convergence for global equilibrium iterations. Accordingly, the contents of the paper are as follows: (i) a description of the kinematics of finite deformation and development of the strain–stress rates, (ii) a brief development of the rate independent plasticity theory for finite strains and a discussion of numerical techniques to integrate the plasticity rate equations, (iii) details of the computational steps to process finite rotations at a material point, development of a consistent tangent operator, and complications arising for the plane–stress idealization. The paper concludes with the solution of several example prob-

lems that illustrate the physically acceptable responses predicted by the material model and the robustness of the numerical implementation. Finite simple extension and shear are examined with comparisons made between analytical and numerical solutions. Severe blunting at a crack–tip is analyzed in the final example with specific attention given to the global convergence rate.

2. KINEMATICS, STRAIN–STRESS MEASURES AND THEIR RATES

Development of the finite strain plasticity model begins with consideration of the deformation gradient

$$\mathbf{F} = \partial \mathbf{x}/\partial \mathbf{X}, \qquad \det(\mathbf{F}) = J > 0 \tag{1}$$

where $\mathbf{X}$ denotes the Cartesian position vectors for material points defined on the reference (undeformed) configuration. Position vectors for material points at time t are denoted $\mathbf{x}$ (configuration $\boldsymbol{B}$ in Fig. 1, after Flanagan and Taylor [8]). The displacements of material points are thus given by $\mathbf{u} = \mathbf{x} - \mathbf{X}$. In static analyses we associate the time–like parameter t with a specified level of loading imposed on the model. Stress and deformation rates are thus defined with respect to the applied loading rather than with time.

The polar decomposition of $\mathbf{F}$ yields

$$\mathbf{F} = \mathbf{VR} = \mathbf{RU} \tag{2}$$

where $\mathbf{V}$ and $\mathbf{U}$ are the left– and right–symmetric, positive definite stretch tensors, respectively; $\mathbf{R}$ is a orthogonal rotation tensor. The principal values of $\mathbf{V}$ and $\mathbf{U}$ are the stretch ratios, λ_i, of the deformation. These two methods for decomposing the motion of a material point are illustrated in Fig. 1. In the initial configuration, $\boldsymbol{B}_o$, we define an orthogonal reference frame at each material point such that the motion relative to these axes is only deformation throughout the loading history. With the $\mathbf{RU}$ decomposition, for example, these axes are "spatial" during the motion from $\boldsymbol{B}_o$ to $\boldsymbol{B}_u$; they are not altered by deformation of the material. However, during the motion from $\boldsymbol{B}_u$ to $\boldsymbol{B}$ these axes are "material"; they rotate with the body in a local average sense at each material point. Strain–stress tensors and their rates referred to these axes are said to be defined in the *unrotated* configuration.

The material derivative of displacement with respect to an applied loading parameter is written as $\mathbf{v} = \dot{\mathbf{x}}$ (i.e., the material point velocity in dynamic analyses). The spatial gradient of this material derivative with respect to the current configuration is given by

$$\mathbf{L} = \frac{\partial \mathbf{v}}{\partial \mathbf{x}} = \frac{\partial \mathbf{v}}{\partial \mathbf{X}} \frac{\partial \mathbf{X}}{\partial \mathbf{x}} = \dot{\mathbf{F}}\mathbf{F}^{-1} \quad . \tag{3}$$

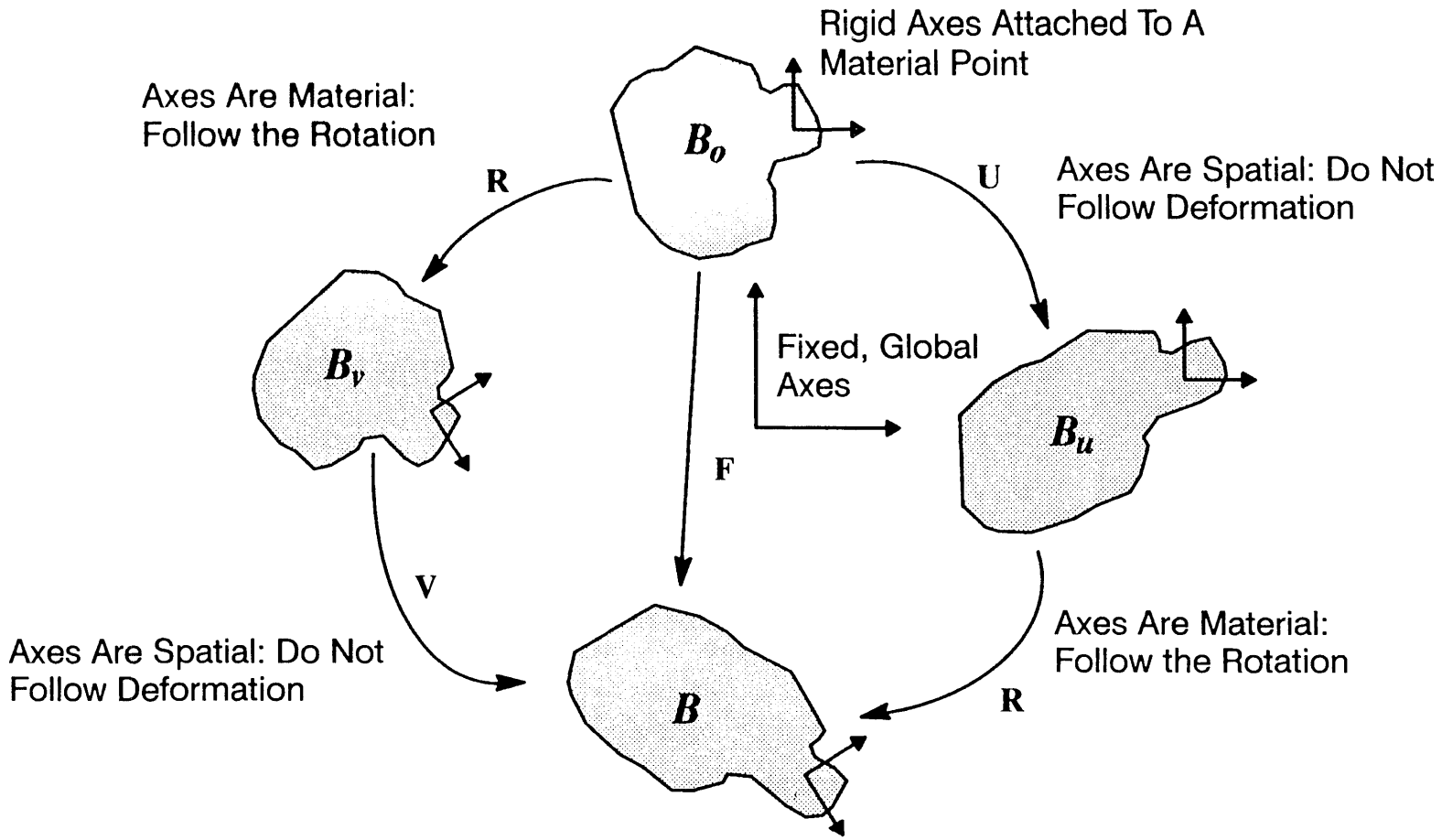

Fig. 1. Initial and deformed configurations illustrating two methods of decomposition.

The symmetric part of **L** is the spatial rate of the deformation tensor, denoted **D**; the skew-symmetric part, denoted **W**, is the spin rate or the vorticity tensor. Thus,

$$\mathbf{L} = \mathbf{D} + \mathbf{W} \tag{4}$$

where

$$\mathbf{D} = \tfrac{1}{2}(\mathbf{L} + \mathbf{L}^T); \qquad \mathbf{W} = \tfrac{1}{2}(\mathbf{L} - \mathbf{L}^T) \ . \tag{5}$$

W represents the rate of rotation of the principal axes of the spatial rate of deformation **D**. When integrated over the loading history, the principal values of **D** are recognized as the logarithmic (true) strains of infinitesimal fibers oriented in the principal directions if the principal directions do not rotate. It is important to note that **D** and **W** have no sense of the deformation history; they are instantaneous rates.

Using the **RU** decomposition of **F**, the spatial gradient **L** may be also written in the form

$$\mathbf{L} = \dot{\mathbf{R}}\mathbf{R}^T + \mathbf{R}\dot{\mathbf{U}}\mathbf{U}^{-1}\mathbf{R}^T \tag{6}$$

in which the following relations are used

$$\dot{\mathbf{F}} = \dot{\mathbf{R}}\mathbf{U} + \mathbf{R}\dot{\mathbf{U}} \tag{7}$$

and

$$\mathbf{F}^{-1} = (\mathbf{R}\mathbf{U})^{-1} = \mathbf{U}^{-1}\mathbf{R}^{-1} = \mathbf{U}^{-1}\mathbf{R}^T \ . \tag{8}$$

The first term in eqn (6) is the rate of rigid–body rotation at a material point and is denoted Ω. The spin rate **W** and Ω are identical when the principal axes of **D** coincide with the principal axes of the current stretch **V**. Simple extension and pure rotation satisfy this condition. The symmetric part of the second term in eqn (6) is called the *unrotated* deformation rate tensor and is denoted **d**

$$\mathbf{d} = \tfrac{1}{2}(\dot{\mathbf{U}}\mathbf{U}^{-1} + \mathbf{U}^{-1}\dot{\mathbf{U}}) \ . \tag{9}$$

The unrotated rate of deformation defines a material strain rate relative to the orthogonal reference frame indicated on configuration ***B*** in Fig. 1.

Using the orthogonality property of **R** that $d(\mathbf{R}^T\mathbf{R})/dt = 0$

$$\mathbf{R}^T\dot{\mathbf{R}} + \dot{\mathbf{R}}^T\mathbf{R} \equiv 0 \tag{10}$$

the unrotated deformation rate may be expressed in the simpler form as

$$\mathbf{d} = \mathbf{R}^T\mathbf{D}\mathbf{R} \quad . \tag{11}$$

The principle of virtual displacements applied in the current ($\boldsymbol{B}$) configuration readily demonstrates the work conjugacy of the the spatial rate of deformation, **D**, and the symmetric Cauchy (true) stress, **T**. Since components of both **D** and **T** are defined relative to the fixed, global axes, the conjugate stress measure for **d** on the unrotated configuration is given simply by

$$\mathbf{t} = \mathbf{R}^T\mathbf{T}\mathbf{R} \tag{12}$$

where **t** is termed the *unrotated* Cauchy stress, i.e., **T** is the tensor **t** expressed on the fixed global axes.

In subsequent sections, finite–element solutions are considered which employ a Total Lagrangian (T.L.) description of the motion [4]. Constitutive quantities **d** and **t** computed on the unrotated configuration must be transformed into stress–strain measures required within the T.L. framework. The T.L. deformation measure is the Green strain given by

$$\mathbf{E} = \tfrac{1}{2}(\mathbf{F}^T\mathbf{F} - \mathbf{I}) \tag{13}$$

which has the rate

$$\dot{\mathbf{E}} = \tfrac{1}{2}(\dot{\mathbf{F}}^T\mathbf{F} + \mathbf{F}^T\dot{\mathbf{F}}) = \mathbf{F}^T\mathbf{D}\mathbf{F} \quad . \tag{14}$$

By using the **RU** decomposition for **F** in eqn (14) and the transformation of eqn (11), the deformation rates are related by

$$\mathbf{d} = \mathbf{U}^{-1}\mathbf{E}\mathbf{U}^{-1} \quad . \tag{15}$$

Upon equating the stress work rates per unit volume in the current($\boldsymbol{B}$) and reference ($\boldsymbol{B_o}$) configurations, the stress measure conjugate to the Green strain rate is determined to be the second Piola–Kirchoff stress, denoted **S**,

$$\mathbf{S} = J\mathbf{F}^{-1}\mathbf{T}\mathbf{F}^{-T} \quad . \tag{16}$$

By substituting the **RU** decomposition of **F** into eqn (16) and using the transformation in eqn (12), we find

$$\mathbf{S} = J\mathbf{U}^{-1}\mathbf{t}\mathbf{U}^{-1} \quad . \tag{17}$$

Finally, we need the relationship between the rates of **t** and **S**. The derivative of **S** yields

$$\dot{\mathbf{S}} = J\mathbf{U}^{-1}\dot{\mathbf{t}}\mathbf{U}^{-1} + tr(\mathbf{D})\mathbf{S} - \mathbf{U}^{-1}\dot{\mathbf{U}}\mathbf{S} - \mathbf{S}\dot{\mathbf{U}}\mathbf{U}^{-1} \tag{18}$$

where *tr*(...) denotes the trace of the symmetric tensor **D**.

3. ELASTO-PLASTIC CONSTITUTIVE FRAMEWORK

3.1 Selection of Strain-Stress Rate

The simplest form of a hypo-elastic constitutive relation is adopted to couple a materially objective stress rate with a work conjugate deformation rate. The Jaumann and Green-Naghdi objective stress rates are

$$\mathbf{T}_J = \dot{\mathbf{T}} - \mathbf{WT} + \mathbf{TW} = \mathbf{C} : \mathbf{D} \tag{19a}$$

$$\mathbf{T}_{GN} = \dot{\mathbf{T}} - \Omega\mathbf{T} + \mathbf{T}\Omega = \mathbf{C} : \mathbf{D} \tag{19b}$$

where the modulus tensor **C** may depend linearly on the current stress tensor and on history dependent state variables. Once the objective stress rate is evaluated using **C** : **D**, the needed spatial rate of Cauchy stress, $\dot{\mathbf{T}}$, is found by computing **W** or Ω and transposing the above equations. In a finite-element setting, these rate expressions are numerically integrated to provide incremental values of the Cauchy stress corresponding to load (time) steps.

When **D** vanishes both the Jaumann and Green-Naghdi rates predicted by the constitutive models also vanish; however, the two stress rates lead to different spatial rates of Cauchy stress since **W** and Ω are generally not identical. Use of the spin tensor **W** in eqn (19a) causes the physically unreasonable response predicted for the finite shear problem; the Green-Naghdi rate leads to a realistic response (see numerical examples below).

The Jaumann rate is adopted extensively in finite-element codes -- the quantity **W** is readily available as a by-product of computing **D** whereas computation of Ω requires polar decompositions of **F**. Hughes and Winget [12] recognized that a constant spin rate **W** (or rotation rate Ω) limits the acceptable step sizes for implicit codes. They developed a numerical integration scheme for eqn (19a) that retains objectivity of the Jaumann rate for rotation increments exceeding 30°. Such refinements, however, do not remove the fundamental cause (**W**) of the oscillatory response in simple shear. Roy, et al. [27] recently implemented a 2-D, implicit finite-element code based on the Green-Naghdi rate as expressed in eqn (19b). They employed the Hughes-Winget procedure to integrate $\mathbf{T}_{GN}$ using Ω computed from polar decompositions of **F** at the start and end of each load increment.

The Green-Naghdi rate may be written alternatively as the rate of *unrotated* Cauchy stress, $\dot{\mathbf{t}}$, expressed on the fixed, Cartesian axes

$$\mathbf{T}_{GN} = \mathbf{R}\dot{\mathbf{t}}\mathbf{R}^T = \mathbf{C} : \mathbf{D} \quad . \tag{20}$$

Transformation of the spatial deformation rate **D** in this expression to the unrotated deformation rate **d** yields

$$\dot{\mathbf{t}} = \mathbf{C} : \mathbf{R}^T\mathbf{D}\mathbf{R} = \mathbf{C} : \mathbf{d} \quad . \tag{21}$$

Constitutive computations, equivalent to the Green–Naghdi rate in eqn (19b), therefore can be performed using stress–strain rates defined on the unrotated configuration. Updated values of **t** are rotated via **R** to obtain the updated Cauchy stress at the end of a load increment. The numerical problems of integrating the rotation rates in eqns (19a) and (19b) are thus avoided. Moreover, internal state variables of the plasticity model, e.g., the back–stress for kinematic hardening, are also defined and maintained on the unrotated configuration and thus never require correction for finite rotation effects. The simplicity derived from this constitutive framework is very appealing and it is adopted in subsequent developments of the finite strain plasticity model. The potential disadvantage of this constitutive framework is the numerical effort to compute **R** for use in eqns (11,12) from the polar decomposition $\mathbf{F}=\mathbf{R}\mathbf{U}$ at thousands of material points for each of many load steps. This issue is discussed in the section on numerical procedures.

3.2 Plasticity Rate Equations

The incremental plasticity theory considered here assumes initial isotropy of the material and neglects strain–rate effects. A von Mises yield surface and associated flow rule are adopted. A mixed isotropic–kinematic hardening model defines subsequent yield surfaces. The Mises yield surface is given by

$$\phi(\mathbf{t}_s', \epsilon_p) = \mathbf{t}_s' \cdot \mathbf{t}_s' - R^2(\bar{\epsilon}_p) \tag{22}$$

where $\mathbf{t}_s'$ is the deviatoric part of the shifted stress vector $\mathbf{t}_s$, R is the radius of the yield surface in deviatoric stress space, and $\bar{\epsilon}_p$ is the effective plastic strain. R is related to the effective tensile stress Y by

$$R = \sqrt{\frac{2}{3}}\, Y(\bar{\epsilon}_p) \tag{23}$$

The shifted stress $\mathbf{t}_s$ is given by

$$\mathbf{t}_s = \mathbf{t} - \mathbf{t}_b \tag{24}$$

where **t** is the current Cauchy stress on the unrotated configuration and $\mathbf{t}_b$ is the back–stress on the unrotated configuration which locates the center of the yield surface (for isotropic hardening, $\mathbf{t}_b = 0$).

Further developments require kinematic decomposition of the total strain rate **d** into elastic and plastic components. The multiplicative decomposition of the deformation gradient

$$\mathbf{F} = \mathbf{F}^e\mathbf{F}^p \tag{25}$$

appears most compatible with the physical basis of elastic–plastic deformation in crystalline metals (see, for example, [3]). $\mathbf{F}^p$ represents plastic flow (dislocations) while $\mathbf{F}^e$ represents lattice distortion; rigid rotation of the material structure may be considered in either term. Substitution of this decomposition into the spatial rate of the displacement gradient eqn (3) yields

$$\mathbf{L} = \dot{\mathbf{F}}^e\mathbf{F}^{-e} + \mathbf{F}^e\dot{\mathbf{F}}^p\mathbf{F}^{-p}\mathbf{F}^{-e} = \mathbf{L}^e + \mathbf{F}^e\mathbf{L}^p\mathbf{F}^{-e} \quad . \tag{26}$$

We now impose the restriction that elastic strains remain vanishingly small compared to the unrecoverable plastic strains; a behavior closely followed by ductile metals having an elastic modulus orders of magnitude greater than the flow stress. Consequently, $\mathbf{F}^p$ and $\mathbf{F}^e$ are uniquely determined by unloading from a plastic state. This considerably simplifies the above expression and permits separate treatment of material elasticity and plasticity. Using the left polar decomposition and writing the stretch as the product of elastic and plastic parts yields

$$\mathbf{F} = \mathbf{F}^e\mathbf{F}^p = \mathbf{V}^e\mathbf{V}^p\mathbf{R} \tag{27}$$

Identifying the elastic deformation as

$$\mathbf{F}^e = \mathbf{V}^e \tag{28}$$

and using the small elastic strain assumption, we have

$$\mathbf{F}^e = \mathbf{I} + \mathbf{e}^e \approx \mathbf{I} \quad . \tag{29}$$

Consequently, the expression for $\mathbf{L}$ is approximated by

$$\mathbf{L} \approx \mathbf{L}^e + \mathbf{L}^p \quad . \tag{30}$$

As in eqn (5), the symmetric part of this approximation for $\mathbf{L}$ is taken as $\mathbf{D}$ with the result that

$$\mathbf{D} \approx \mathbf{D}^e + \mathbf{D}^p \quad . \tag{31}$$

Given the restriction of vanishingly small elastic strains, the multiplicative decomposition of the deformation gradient in eqn (25) leads to the familiar additive decomposition of the spatial deformation rate $\mathbf{D}$ into elastic and plastic components. The conversion of $\mathbf{D}$ to the unrotated configuration using eqn (11) provides the decomposition scheme needed for $\mathbf{d}$ as

$$\mathbf{d} = \mathbf{R}^T(\mathbf{D}^e + \mathbf{D}^p)\mathbf{R} = \mathbf{d}^e + \mathbf{d}^p \quad . \tag{32}$$

Once the above transformation of elastic and plastic strain rates onto the unrotated configuration is accomplished, remaining steps in development of the finite–strain plasticity theory are identical to those for classical small–strain theory.

If the elastic strains are not vanishingly small, the incrementally linear form of this hypo–elastic material model predicts hysteretic dissipation and residual stresses for some closed loading paths, for example, the path defined by finite extension → finite shear → tension unloading → shear unloading [18]. Uncoupled loading–unloading for extension and shear produces no residual stresses. For finite–strain plasticity of ductile metals having large modulus–to–yield stress ratios this situation is not a serious concern since plastic strains are commonly 50–100 times greater than the elastic strains.

3.3 Stress Updating on the Unrotated Configuration

The plasticity rate equations are numerically integrated over a finite time (load) increment using the elastic predictor–radial return algorithm [7,16,19,29,30]. Because integration of the stress rate occurs with all quantities cast onto the unrotated configuration, algorithmic details of the integration procedure are identical to those developed for conventional small–strain plasticity models. The elastic predictor–radial return method provides the most accuracy for both single step and subincrementation schemes (the strain increment is divided into m subincrements with the plasticity integration procedure applied successively over each subincrement). Moreover, the procedure is unconditionally stable and mixed isotropic–kinematic hardening is easily included.

The plane–stress idealization introduces additional complexities at two levels. First, the (u,v) nodal displacements do not provide a means to compute the through–thickness strain increment, Δd_{33}. The updated stress t_{33} must be zero yet non–zero values of the back stress, $t_{33(b)}$, and the shifted stress, $t_{33(s)}$, are required to match the Bauschinger effect predicted by a corresponding 3–D model defined with plane–stress boundary conditions. The elastic predictor–radial return algorithm, for example, can be executed iteratively in a 3–D setting to compute simultaneously Δd_{33} and the updated stresses under the constraint that $t_{33} \rightarrow 0$. Simo and Taylor [31] and Keppel and Dodds [16] provide details of two such schemes. The second complication introduced by plane–stress involves the F_{33} term of the deformation gradient which accounts for finite changes of material thickness due to loading. This term must be constructed from increments of Δd_{33} determined by the stress update procedure. Computation of F_{33} is described in the next section.

4. NUMERICAL PROCEDURES FOR FINITE STRAINS

The numerical algorithms in this section are developed for a Total Lagrangian setting. Only minor modifications are required for use of these same algorithms in an Updated

Lagrangian setting. The global solution is advanced from time (load) t_n to t_{n+1} using an incremental–iterative Newton method. Iterations at t_{n+1} to remove unbalanced nodal forces are conducted under fixed external loading and no change in the prescribed displacements for displacement controlled loading. Each such iteration, denoted i, provides a revised estimate for the total displacements at t_{n+1}, denoted $\mathbf{u}_{n+1}^{(i)}$. Fully converged displacements at t_n are denoted $\mathbf{u}_n$. Following Pinsky, et al. [23] a mid–increment scheme is adopted in which deformation rates are evaluated on the intermediate configuration at $\frac{1}{2}(\mathbf{u}_n + \mathbf{u}_{n+1}^{(i)}) = \mathbf{u}_{n+\frac{1}{2}}^{(i)}$. The choice of 0.5 represents a specific form of the generalized trapezoidal rule that is unconditionally stable and second–order accurate. Key and Krieg [17] have demonstrated the optimality of the mid–point configuration for integrating the rate of deformation and the resulting correspondence with logarithmic strain.

The following sections describe the computational processes performed at each material (Gauss) point to: 1) update stresses, 2) provide a consistent tangent matrix for updating the global stiffness matrix and 3) resolve complications arising from the plane–stress idealization. A brief discussion of the procedure to compute the polar decomposition of the deformation gradient is also provided. The organization of a particular finite–element code dictates which operations are performed in the element dependent routines and which are performed in the material models; thus no particular distinction is made here. Standard finite–element procedures to compute deformation gradients at Gauss points in a T.L. setting are also omitted.

4.1 Stress Updating Procedure

The computational steps are:

Step 1. Compute the deformation gradients at $n + \frac{1}{2}$ and $n + 1$

$$\mathbf{F}_{n+1}^{(i)} = \frac{\partial(\mathbf{X} + \mathbf{u}_{n+1}^{(i)})}{\partial \mathbf{X}}; \qquad J_{n+1}^{(i)} = \det(\mathbf{F}_{n+1}^{(i)}) \tag{33}$$

$$\mathbf{F}_{n+\frac{1}{2}}^{(i)} = \frac{\partial(\mathbf{X} + \mathbf{u}_{n+\frac{1}{2}}^{(i)})}{\partial \mathbf{X}} \tag{34}$$

Step 2. Compute polar decompositions at $n + \frac{1}{2}$ and $n + 1$

$$\mathbf{F}_{n+1}^{(i)} = \mathbf{R}_{n+1}^{(i)} \cdot \mathbf{U}_{n+1}^{(i)} \tag{35}$$

$$\mathbf{F}_{n+\frac{1}{2}}^{(i)} = \mathbf{R}_{n+\frac{1}{2}}^{(i)} \cdot \mathbf{U}_{n+\frac{1}{2}}^{(i)} \tag{36}$$

Step 3. Compute the i th estimate for the spatial gradient of the displacement increment over the step

$$\Delta \mathbf{L}^{(i)} = \Delta \mathbf{F}^{(i)} \cdot \mathbf{F}_{n+\frac{1}{2}}^{(i)-1} \tag{37}$$

where

$$\Delta \mathbf{F}^{(i)} = \frac{\partial(\mathbf{u}_{n+1}^{(i)} - \mathbf{u}_n)}{\partial \mathbf{X}} = \frac{\partial(\Delta \mathbf{u}^{(i)})}{\partial \mathbf{X}} \tag{38}$$

Step 4. Compute the i th estimate for the spatial deformation increment over the step

$$\Delta \mathbf{D}^{(i)} = \tfrac{1}{2}[\Delta \mathbf{L}^{(i)} + \Delta \mathbf{L}^{(i)T}] \tag{39}$$

Step 5. Rotate the increment of spatial deformation to the unrotated configuration

$$\Delta \mathbf{d}^{(i)} = \mathbf{R}_{n+\frac{1}{2}}^{(i)T} \cdot \Delta \mathbf{D}^{(i)} \cdot \mathbf{R}_{n+\frac{1}{2}}^{(i)} \tag{40}$$

Step 6. The terms of $\Delta \mathbf{d}^{(i)}$ define the strain increments for use in a conventional small–strain plasticity model. Invoke the small–strain plasticity model to provide the i th estimate for the unrotated Cauchy stress at $n+1$

$$\mathbf{t}_{n+1}^{(i)} \leftarrow \mathbf{C}(\mathbf{t}_n, \bar{\epsilon}_{p(n)}, \mathbf{t}_{b(n)}, \Delta \mathbf{d}^{(i)}) \tag{41}$$

where $\mathbf{C}$ denotes the small–strain integration process using the elastic–predictor, radial return algorithm. The integration process requires state variables at n: the unrotated Cauchy stress, the equivalent plastic strain, and the back–stresses on the unrotated configuration.

Step 7. The unrotated Cauchy stress at $n+1$ is transformed to the 2nd Piola–Kirchoff stress at $n+1$ as required for the T.L. setting

$$\mathbf{S}_{n+1}^{(i)} = J_{n+1}^{(i)} \cdot \mathbf{U}_{n+1}^{(i)-1} \cdot \mathbf{t}_{n+1}^{(i)} \cdot \mathbf{U}_{n+1}^{(i)-1} \tag{42}$$

Key advantages of the above steps are the absence of half–angle rotations applied to stresses (and back–stresses) found in co–rotational rate formulations, eqn (19), and most importantly, the ability to use an existing small–strain plasticity model for *Step* 6 without modification since all quantities are referred to the unrotated configuration. The disadvantage is the need to perform two polar decompositions for each stress update.

Finally, converged deformation increments $\Delta \mathbf{D}$ are summed over k load steps to define the logarithmic strains for output

$$e_{ij} = \sum_{n=1}^{n=k} \Delta D_{ij} \tag{43}$$

4.2 Tangent Modulus for Stiffness Updating

A tangent modulus matrix, denoted $[\mathbf{C}_{ep}]$, is needed to form the element–structure stiffness matrix in implicit codes. The moduli couple increments of Green strain with increments of 2nd Piola–Kirchoff stress required by the T.L. formulation. To maintain a quadratic convergence rate of the global Newton iterations, the tangent operator must be consistent with the numerical algorithm employed to integrate the stress rate just described. Consistency implies that the finite stress increment predicted by the tangent oper-

ator acting on a strain increment matches, to first order, the stress increment predicted by the integration procedure.

The small–strain plasticity model provides the consistent tangent modulus [30] that relates the unrotated stress increments and unrotated deformation increments (in matrix–vector form)

$$\{\Delta \mathbf{t}\} = \left[\mathbf{C}^{*}_{ep}\right] \{\Delta \mathbf{d}\} \quad . \tag{44}$$

The needed form of the above relation for the global T.L. approach is

$$\{\Delta \mathbf{S}\} = [\mathbf{C}_{ep}] \{\Delta \epsilon_G\} \tag{45}$$

where $\{\Delta \epsilon_G\}$ is the incremental Green strain. To transform $[\mathbf{C}^{*}_{ep}] \rightarrow [\mathbf{C}_{ep}]$, the incremental forms of the rate transformations in eqns (15) and (18) are employed

$$\Delta \mathbf{S} = J\ \mathbf{U}^{-1}\Delta \mathbf{t}\ \mathbf{U}^{-1} + tr(\Delta \mathbf{D})\mathbf{S} - \mathbf{U}^{-1}\Delta \mathbf{U}\ \mathbf{S} - \mathbf{S}\Delta \mathbf{U}\mathbf{U}^{-1} \tag{46}$$

where $tr(..)$ denotes the trace of a tensor and

$$\Delta \mathbf{d} = \mathbf{U}^{-1}\Delta \epsilon_G\ \mathbf{U}^{-1} \quad . \tag{47}$$

Attempts to combine eqns (46) and (47) into a transformation operator yield a non–symmetric $[\mathbf{C}_{ep}]$ even though $[\mathbf{C}^{*}_{ep}]$ is symmetric. Moreover, the resulting expression is unnecessarily complex and very difficult to express in the matrix form of eqn (45). To preserve the symmetry of $[\mathbf{C}_{ep}]$, two assumptions are made to develop an approximate transformation operator: (1) the material is incompressible such that $tr(\Delta \mathbf{D}) \rightarrow 0$ and (2) the term $\Delta \mathbf{U}$ may be neglected in comparison to **U** and **S**. With these two assumptions, the approximate transformation of tangent moduli may be written in matrix form as

$$\left[\mathbf{C}_{ep}\right] \approx J \cdot [\mathbf{T}] \cdot \left[\mathbf{C}^{*}_{ep}\right] \cdot [\mathbf{T}]^{T} \quad . \tag{48}$$

Terms of the 6x6 matrix [**T**] (for 3–D) are derived from the symmetric, positive definite matrix **U** computed from the polar decomposition $\mathbf{F} = \mathbf{RU}$ at the current configuration. The 3–D form of [**T**] is given below. Axisymmetric and 2–D specializations are derived by omitting the appropriate rows and columns. The row–column ordering of [**T**] is: *x, y, z, xy, yz, xz*. To shorten the notation, we introduce the following terms:

$$u_1 = U^{-1}_{11};\quad u_2 = U^{-1}_{21};\quad u_3 = U^{-1}_{22};\quad u_4 = U^{-1}_{31};\quad u_5 = U^{-1}_{32};\quad u_6 = U^{-1}_{33} \quad . \tag{49}$$

With this notation, [T] is given by

$$[\mathbf{T}] = \begin{bmatrix} u_1^2 & u_2^2 & u_4^2 & 2u_1u_2 & 2u_2u_4 & 2u_1u_4 \\ u_2^2 & u_3^2 & u_5^2 & 2u_2u_3 & 2u_3u_5 & 2u_2u_5 \\ u_4^2 & u_5^2 & u_6^2 & 2u_4u_5 & 2u_5u_6 & 2u_4u_6 \\ u_1u_2 & u_2u_3 & u_4u_5 & u_1u_3 + u_2^2 & u_4u_3 + u_2u_5 & u_1u_5 + u_2u_4 \\ u_2u_4 & u_3u_5 & u_5u_6 & u_2u_5 + u_4u_3 & u_3u_6 + u_5^2 & u_2u_6 + u_4u_5 \\ u_1u_4 & u_2u_5 & u_4u_6 & u_1u_5 + u_2u_4 & u_2u_6 + u_4u_5 & u_1u_6 + u_4^2 \end{bmatrix} \tag{50}$$

Numerical tests demonstrate that this approximate transformation of tangent moduli maintains the convergence rate of the global Newton iterations (subsequently discussed example problems show this). Use of the *consistent* moduli for the unrotated configuration in eqn (44) appears more important for good convergence rates than the purely geometric transformation approximated by eqn (48).

4.3 Plane–Stress Idealization

The F_{31}, F_{32}, F_{13}, and F_{23} terms of **F** vanish for motion restricted to the 1–2 plane (plane–stress, plane–strain, and axisymmetric idealizations). The F_{11}, F_{12}, F_{21}, and F_{22} terms are determined from the in–plane displacements. The F_{33} term is necessary for computation of $J =$ det(**F**); J appears in the stress and tangent moduli transformations, eqns (42) and (43). For plane–strain analyses $F_{33} = 1$; for axisymmetric analyses $F_{33} = (R_o + u)/R_o$ where R_o is the undeformed radius of the material point.

For plane–stress conditions, F_{33} is simply the current thickness, T, divided by the undeformed thickness, T_o,

$$F_{33} = \frac{T}{T_o} = \frac{T_o + \Delta T}{T_o} \quad . \tag{51}$$

The change in thickness is obtained by integrating the unrotated deformation rate over the loading history to define the through–thickness logarithmic strain

$$\ln(1 + \frac{\Delta T}{T_o}) = e_{33} = \int d_{33} = \int D_{33} \approx \sum \Delta d_{33} \tag{52}$$

where equivalence of the (3,3) spatial deformation and (3,3) unrotated deformation terms is noted for motion in the 1–2 plane. The solution of the above expression for ΔT and the substitution into eqn (51) provides the needed expression for F_{33} as

$$F_{33} = \exp(e_{33}) \quad . \tag{53}$$

The term $\sum \Delta d_{33}$ is maintained as a history dependent quantity at each Gauss point in the same manner as the accumulated plastic strain $\bar{\epsilon}_p$.

4.4 Polar Decomposition

The polar decomposition $\mathbf{F} = \mathbf{RU}$ is a key step in the stress–updating algorithm and must be performed twice for each Gauss point for each stress update, i.e., at $n + \frac{1}{2}$ and $n + 1$. The computational effort required for the polar decomposition should be insignificant relative to the element stiffness computation and the equation solving effort. For their explicit code, Flanagan and Taylor [8] developed an algorithm for the integration of $\dot{\mathbf{R}} = \boldsymbol{\Omega}\mathbf{R}$ that maintains orthogonality of $\mathbf{R}$ for the very small displacement increments characteristic of explicit solutions. Numerical tests readily show their procedure fails for large displacement increments experienced with implicit global solutions. The following algorithm removes such approximations and yet remains computationally very efficient with the framework of an implicit solution.

Step 1. Compute the right Cauchy–Green tensor

$$\mathbf{C} = \mathbf{F}^T\mathbf{F} \tag{54}$$

and its square

$$\mathbf{C}^2 = \mathbf{C}^T\mathbf{C} \tag{55}$$

where only the upper–triangular form of the symmetric products (6 terms) are actually computed and stored.

Step 2. Compute the eigenvalues λ_1^2, λ_2^2 and λ_3^2 of $\mathbf{C}$. A Jacobi transformation procedure specifically designed for 3x3 matrices is used to extract the eigenvalues. Do–loops are eliminated by explicitly coding each off–diagonal rotation form. Two or, at most, three sweeps are needed to obtained eigenvalues converged to a 10^{-6} tolerance.

Step 3. Compute invariants of $\mathbf{U}$ and the det($\mathbf{F}$)

$$I_U = \lambda_1 + \lambda_2 + \lambda_3 \tag{56a}$$

$$II_U = \lambda_1\lambda_2 + \lambda_2\lambda_3 + \lambda_1\lambda_3 \tag{56b}$$

$$III_U = \lambda_1\lambda_2\lambda_3 = J = det(\mathbf{F}) \tag{56c}$$

Step 4. Form the upper triangle of the symmetric, right stretch, $\mathbf{U}$, and it's symmetric inverse, $\mathbf{U}^{-1}$ (see [11])

$$\mathbf{U} = \beta_1(\beta_2\mathbf{I} + \beta_3\mathbf{C} - \mathbf{C}^2) \tag{57a}$$

where $\mathbf{I}$ denotes a unit tensor with the β coefficients defined by

$$\beta_1 = 1/(I_U II_U - III_U), \quad \beta_2 = I_U III_U, \quad \beta_3 = I_U^2 - II_U \tag{57b}$$

Similarly, the inverse of **U** may be formed directly as

$$\mathbf{U}^{-1} = \gamma_1(\gamma_2\mathbf{I} + \gamma_3\mathbf{C} + \gamma_4\mathbf{C}^2) \tag{57c}$$

where the γ coefficients defined by

$$\gamma_1 = 1/III_u(I_U II_U - III_U), \quad \gamma_2 = I_U II_U^2 - III_U(I_U^2 + II_U), \tag{57d}$$

$$\gamma_3 = -III_U - I_U(I_U^2 - 2II_U), \quad \gamma_4 = I_U$$

Step 5. Form **R** as the product

$$\mathbf{R} = \mathbf{F}\mathbf{U}^{-1} \tag{58}$$

The FORTRAN code listing for the above procedure is given in the appendix. Table 1 summarizes the relative computational effort required for (1) generation of the element tangent stiffness matrix, (2) stress updating at all Gauss points of the element (including two polar decompositions at each Gauss point), and (3) the relative time required for a single polar decomposition. Results are given for an axisymmetric, 8–node isoparametric element and a 3–D, 20–node isoparametric brick element. Both elements employ reduced integration rules; 2x2 for the axisymmetric element and 2x2x2 for the 3–D element. Computations were performed on a Unix workstation. The CPU time required for generation of the element tangent stiffness is assigned a unit value for each case. The results clearly demonstrate that polar decompositions are not a computational issue in an implicit code.

Table 1. Relative Computational Effort Required for Polar Decompositions

Computation	8–Node Axisymmetric (2x2 Gauss Rule)	20–Node 3–D (2x2x2 Gauss Rule)
Element $[K_T]$	1.0	1.0
Element Stress Updating	0.46	0.15
Single Polar Decomposition	0.01	0.0005

5. NUMERICAL EXAMPLES

Numerical results for three example problems are presented in this section. The examples demonstrate the excellent performance of the finite strain model for both 2–D and 3–D

configurations. The first two examples consider finite, homogeneous deformation in uncoupled extension and simple shear. By adopting an incrementally–linear material, analytical solutions may be constructed for these two problems to assess the accuracy of the finite–element solutions. The third example considers the plane–strain, Mode I small–scale yielding problem for a material that follows the rate independent, incremental plasticity theory. An initially blunt notch tip is opened to several times the initial width in a boundary layer model that approximates the conditions at a crack tip in an infinite body The finite–strain model is implemented as a pre– and post– processor for the existing small–strain plasticity model in our research finite–element system (POLO–FINITE [6]). The small–strain model required no changes; we consider this to be a significant advantage of adopting the unrotated configuration to perform constitutive computations.

5.1 Homogeneous Finite Extension

Consider a unit block of material aligned with edges parallel to the coordinate axes (see Fig. 2). The block is constrained and loaded consistent with uniaxial tension in the X_1 direction. The displacement field is given by

$$u_1 = aX_1t, \qquad u_2 = kaX_2t, \qquad u_3 = kaX_3t \tag{59}$$

where a, k are constants and t is a time–like loading parameter that increases monotonically from zero. For a unit cube, a may be taken as unity. The coordinate stretch ratios are then

$$\lambda_i = (X_i + u_i)/X_i \quad . \tag{60}$$

In the absence of rotation, the unrotated Cauchy, Jaumann, and Green–Naghdi stress rates are identical, i.e., $\mathbf{R}=\mathbf{I}$, $\mathbf{F}=\mathbf{U}$, $\mathbf{d}=\mathbf{D}$, and $\mathbf{W}=\mathbf{0}$. The hypo–elastic relations all have the form

$$\dot{\mathbf{t}} = \lambda \mathbf{I} tr(\mathbf{d}) + 2\mu \mathbf{d} \tag{61}$$

where λ and μ are the Lame constants. Direct integration of these relations yields

$$t_{11} = E \ln \lambda_1, \qquad t_{22} = t_{33} = 0 \tag{62}$$

for the Cauchy stresses. The stretch ratios are related by

$$\ln \lambda_2 = \ln \lambda_3 = -\nu \ln \lambda_1 \tag{63}$$

from which the corresponding axial force is found to be (for a cube with unit initial edge lengths)

$$P_1 = \lambda_1^{-2\nu} E \ln \lambda_1 \tag{64}$$

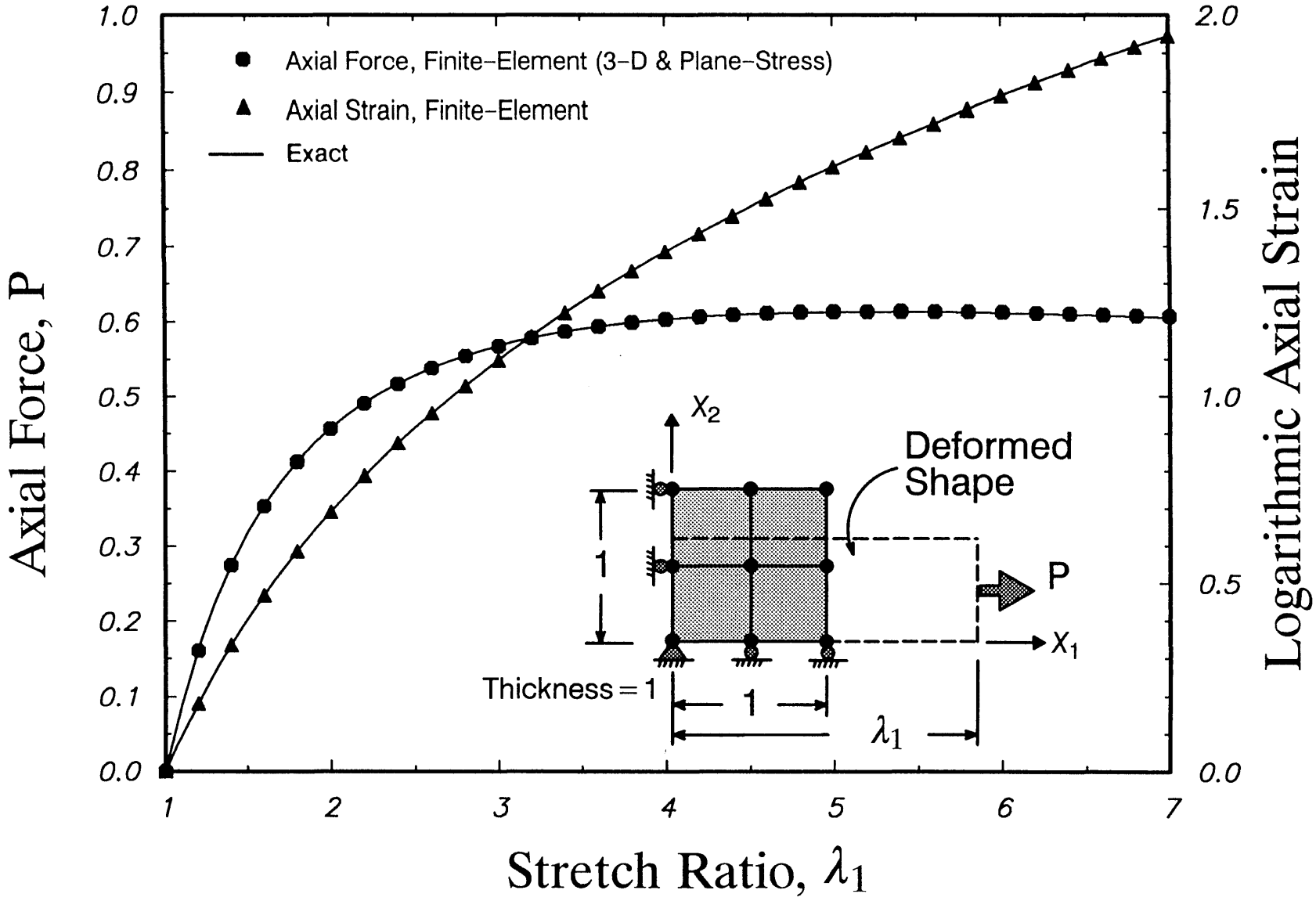

Fig. 2. Homogeneous finite extension. Comparison of finite-element results with analytical solutions. Incremental, linear-elastic material: $E = 1$, $\nu = 0.3$.

where E and ν are Young's modulus and Poisson's ratio, respectively. This load–stretch response, plotted in Fig. 2, exhibits a maximum load effect $\partial P_1/\partial\lambda_1 = 0$ at a critical stretch ratio of $\lambda_1 = 5.29$.

Plane–stress and 3–D finite–element models are analyzed for this finite extension problem. The plane–stress model contains four, linear quadrilateral elements; the 3–D model contains eight, linear brick elements. The integration order for the plane–stress elements is 2x2 with a 2x2x2 order used for the 3–D elements. Constitutive computations are performed by the incremental plasticity model with a yield stress large enough to prevent plastic deformation. Numerical results for these two models should be identical provided the through–thickness strain computations described in eqns (51) and (53) are performed during solution of the plane–stress model. Both models are loaded by displacements imposed on the face $X_1 = 1$. Thirty (30) equal size increments are imposed to reach the deformation $\lambda_1 = 7$. Iterations at each load step are performed until the convergence test given by

$$\| \mathbf{R} \| \leq \| \mathbf{P} \| * 10^{-4} \tag{65}$$

is satisfied, where $\| \ \|$ denotes the Euclidean norm, **R** is the residual force vector, and **P** is the vector of total reactions at the constrained nodes. For both the plane–stress and 3–D solutions, a total of 60 iterations are performed for the 30 load steps; two iterations are needed for convergence at each load step. The plane–stress and 3–D solutions are identical. Figure 2 compares the analytical and computed axial forces as a function of the stretch ratio. The figure also compares the exact axial strain, $\ln\lambda_1$, with the finite–element approximation obtained by summing deformation increments as in eqn (43). The maximum error in predicted axial force is 0.3% while the maximum error in the predicted logarithmic strain is 0.1%.

5.2 Homogeneous Finite Shear

In the finite simple shear problem discussed by Dienes [5], material undergoes simultaneous stretching and large rotation. Analytical solutions for each stress rate are now available for assessment of numerical implementations. A unit cube of material is again employed as shown in Fig. 3. The displacement field is given by

$$u_1 = aX_2t, \qquad u_2 = u_3 = 0 \tag{66}$$

where a is a constant and t is a time–like loading parameter that increases monotonically from zero. The deformation gradient and material displacement derivative are simply

$$\mathbf{F} = \begin{bmatrix} 1 & at & 0 \\ 0 & 1 & 0 \\ 0 & 0 & 1 \end{bmatrix} \qquad \mathbf{L} = \begin{bmatrix} 0 & a & 0 \\ 0 & 0 & 0 \\ 0 & 0 & 0 \end{bmatrix} . \tag{67}$$

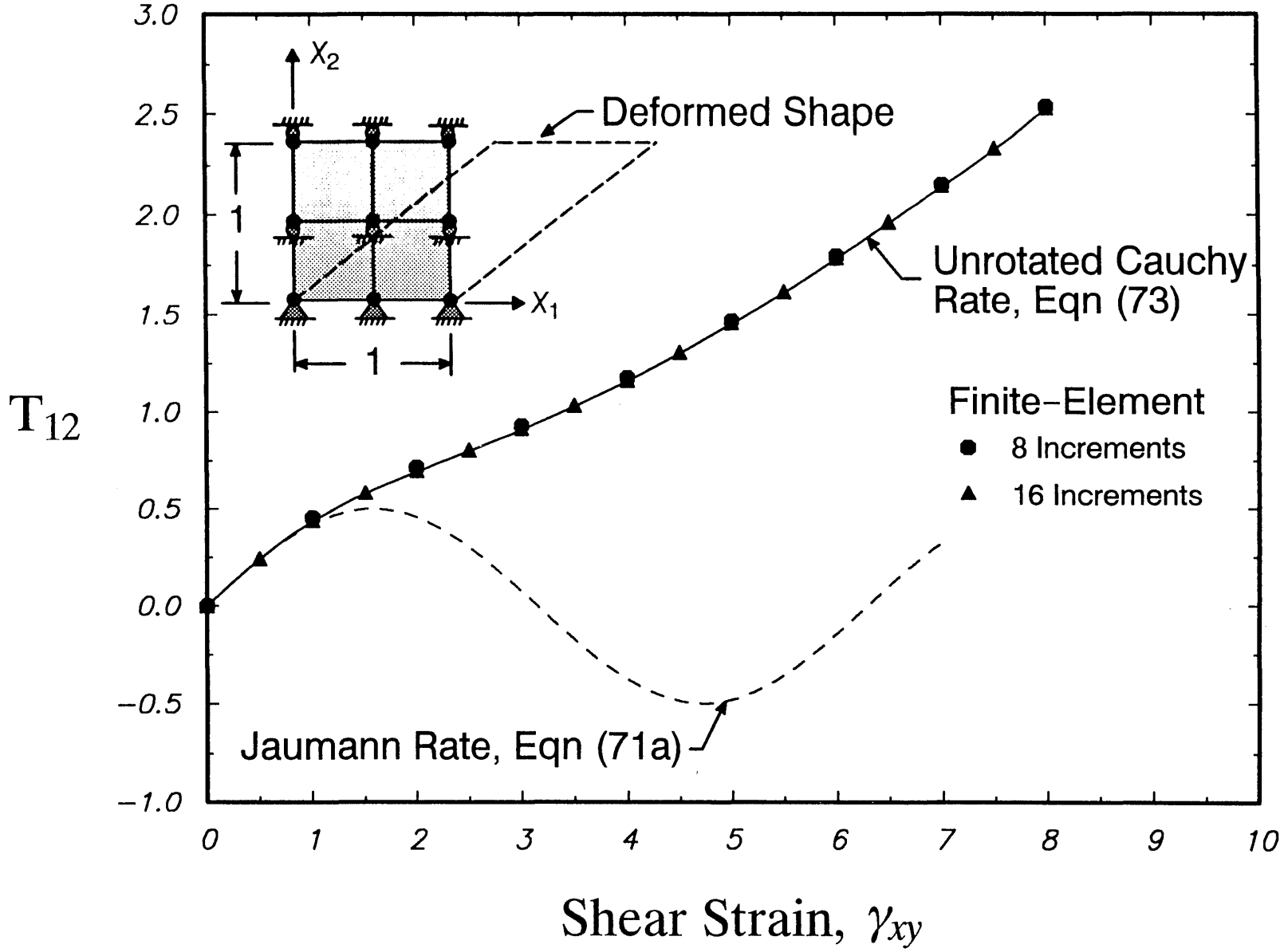

Fig. 3a. Homogeneous finite simple shear. Comparison of finite-element and analytical solutions for the Cauchy shear stress. Incremental, linear-elastic material: $E=1$, $\nu=0.3$.

F shows that the deformation is isochoric with $J = 1$. Since motion is restricted to the X_1–X_2 plane, **R** must have the form

$$\mathbf{R} = \begin{bmatrix} \cos\beta & \sin\beta & 0 \\ -\sin\beta & \cos\beta & 0 \\ 0 & 0 & 1 \end{bmatrix} \tag{68}$$

where the angle β is given by

$$\beta = \tan^{-1}(at/2) \quad . \tag{69}$$

The rate of deformation in the fixed Cartesian system, eqn (5), and the unrotated configuration, eqn (11), are

$$\mathbf{D} = \frac{a}{2}\begin{bmatrix} 0 & 1 & 0 \\ 1 & 0 & 0 \\ 0 & 0 & 0 \end{bmatrix} \qquad \mathbf{d} = \frac{a}{2}\begin{bmatrix} -\sin 2\beta & \cos 2\beta & 0 \\ \cos 2\beta & \sin 2\beta & 0 \\ 0 & 0 & 0 \end{bmatrix} \quad . \tag{70}$$

Dienes [5] adopted the incrementally–linear, eqn (61), for the Jaumann and unrotated stress rates. The constitutive models are thus

$$\mathbf{T}_J = \lambda \mathbf{I} tr(\mathbf{D}) + 2\mu \mathbf{D} \tag{71a}$$

$$\mathbf{t} = \lambda \mathbf{I} tr(\mathbf{d}) + 2\mu \mathbf{d} \tag{71b}$$

The integration of eqn (71a) yields the following solution for the Cauchy stresses

$$T_{11} = -T_{22} = \mu(1 - \cos at), \qquad T_{12} = \mu \sin at \tag{72a}$$

while the integration of eqn (71b) yields the unrotated Cauchy stresses as

$$t_{11} = -t_{22} = 4\mu ln(\cos\beta), \qquad t_{12} = 2\mu(2\beta - \tan\beta) \tag{72b}$$

These stresses are rotated to the fixed Cartesian system using **R** from eqn (68) to yield

$$T_{11} = -T_{22} = 4\mu[\cos 2\beta ln(\cos\beta) + \beta \sin 2\beta - \sin^2\beta],$$

$$T_{12} = 2\mu \cos 2\beta[2\beta - 2\tan 2\beta \ln(\cos\beta) - \tan\beta] \tag{73}$$

Figure 3 compares the analytical solutions for the Cauchy stresses obtained using the Jaumann rate and the unrotated Cauchy rate. The solution for the Jaumann rate exhibits a physically unacceptable harmonic oscillation while the solution for the unrotated

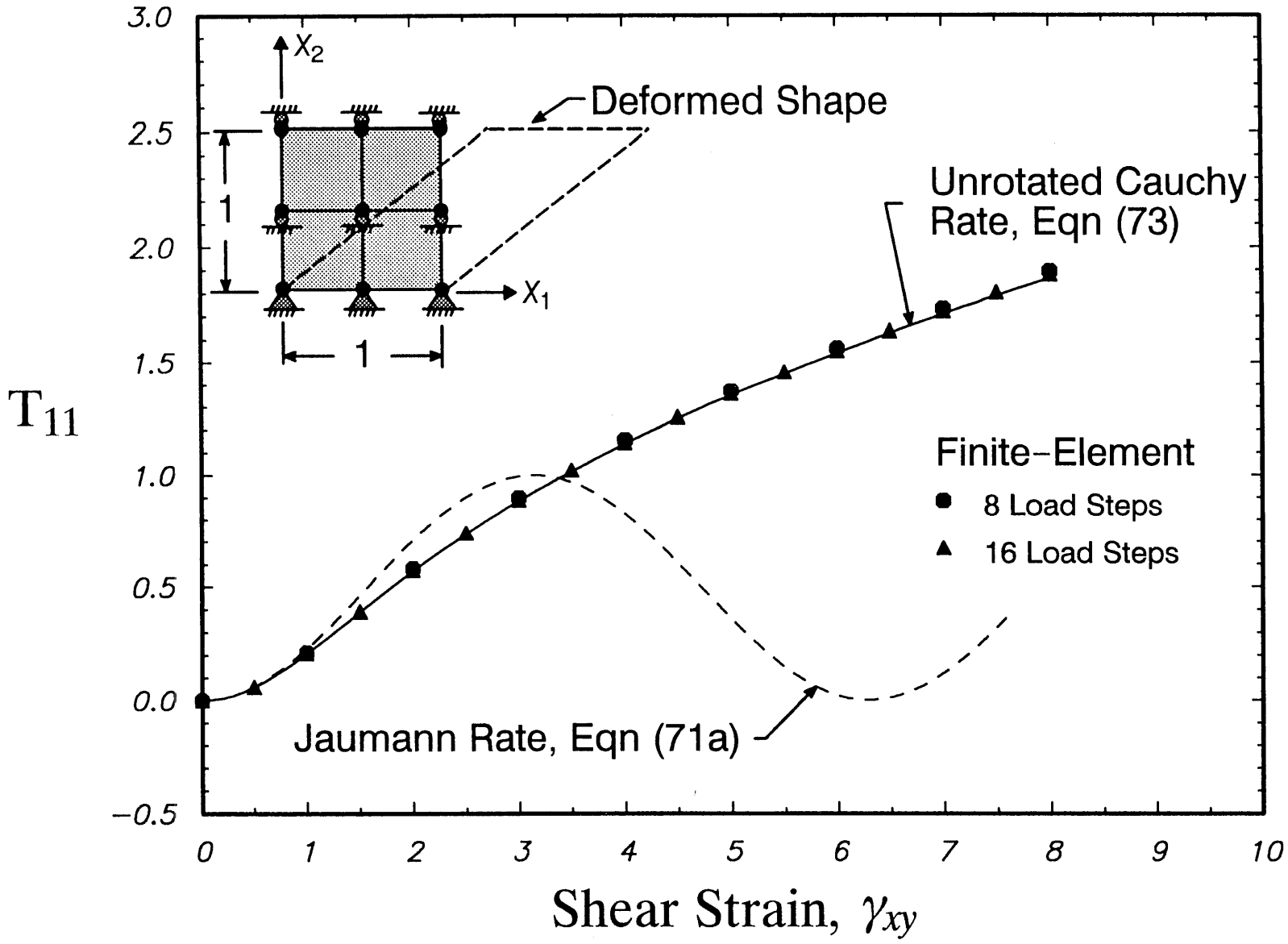

Fig. 3b. Homogeneous finite simple shear. Comparison of finite-element and analytical solutions for the Cauchy normal stress. Incremental, linear-elastic material: $E=1$, $\nu=0.3$.

Cauchy rate increases monotonically with increasing deformation. The Green–Naghdi rate yields the same solution for the stresses as eqn (73).

The finite–element model for the finite shear problem contains four, linear quadrilateral elements with an integration order of 2x2. To maintain the isochoric deformation described by eqn (66), the model must be loaded by prescribing the displacements at all nodes. Thus no iterations are necessary. The logarithmic shear strain, γ_{xy}, is increased to a magnitude of 8 in separate analyses using 8 and 16 equal size displacement increments. For a unit cube, the shear strain equals the imposed displacement along the edge $X_2 = 1$. The computed Cauchy stresses for these analyses are compared with the exact solutions in Fig. 4. The finite–element stresses very closely match the exact solution and show very minor dependence on the load–step magnitude. In the first of 8 increments, the error is 3%; as $\gamma_{xy} \to 8$ the error decreases to less than 0.1%.

5.3 Crack–Tip Blunting In Small–Scale Yielding

Small–scale yielding (SSY) in Mode I plane–strain characterizes the deformation near a crack tip in an infinite body. Rice and Tracey [26] and McMeeking [20,21] developed a boundary–layer approximation for the infinite body model that is suitable for finite–element analysis. The SSY model consists of an annular region containing either a sharp or smoothly blunt crack tip which is subjected to increasing displacements of the elastic (Mode I) singular field on the outer circular boundary. SSY models are commonly employed in fracture mechanics studies to investigate continuum based, micromechanics parameters that describe the initiation of ductile crack growth. Very efficient finite–element models that include the effects of large strains and large material rotation are essential for studies that investigate such parameters.

Figure 4 shows the inner portion of the plane–strain finite–element model developed to solve the SSY problem. The crack is modeled as a notch of initial width b_o having a semi–circular tip. The mesh extends to a radius $R = 5000 b_o$ and contains 2328 nodes, 737 8–node isoparametric elements. The smallest element at the notch tip has length $b_o/12$. The use of reduced (2x2) integration eliminates locking due to the incompressible plastic deformation. The uniaxial, true stress–logarithmic strain curve follows a power–law form

$$\epsilon/\epsilon_o = \sigma/\sigma_o + \alpha(\sigma/\sigma_o)^n \tag{74}$$

where the material constants selected for analysis are: $\epsilon_o = 0.002, \sigma_o = 60$, $n = 10$, $\alpha = 1$, and Poisson's ratio $\nu = 0.3$. Symmetrical boundary conditions are applied on the crack plane ($X_1 \geq b_o$, $X_2 = 0$). The notch surface remains traction free. Displacement increments of the elastic K_I–field for Mode I are imposed on the outer circular boundary. The boundary displacements are increased monotonically in 40 equal increments to the level $K_I^2/(\sigma_o^2 R) = 1.11$ at which point the plastic zone extends $\approx R/10$. Iterations at fixed K_I are performed until the convergence test, eqn (65), with a tolerance of 5×10^{-4} is satisfied. This tolerance insures 0.1% convergence of the strains for this problem.

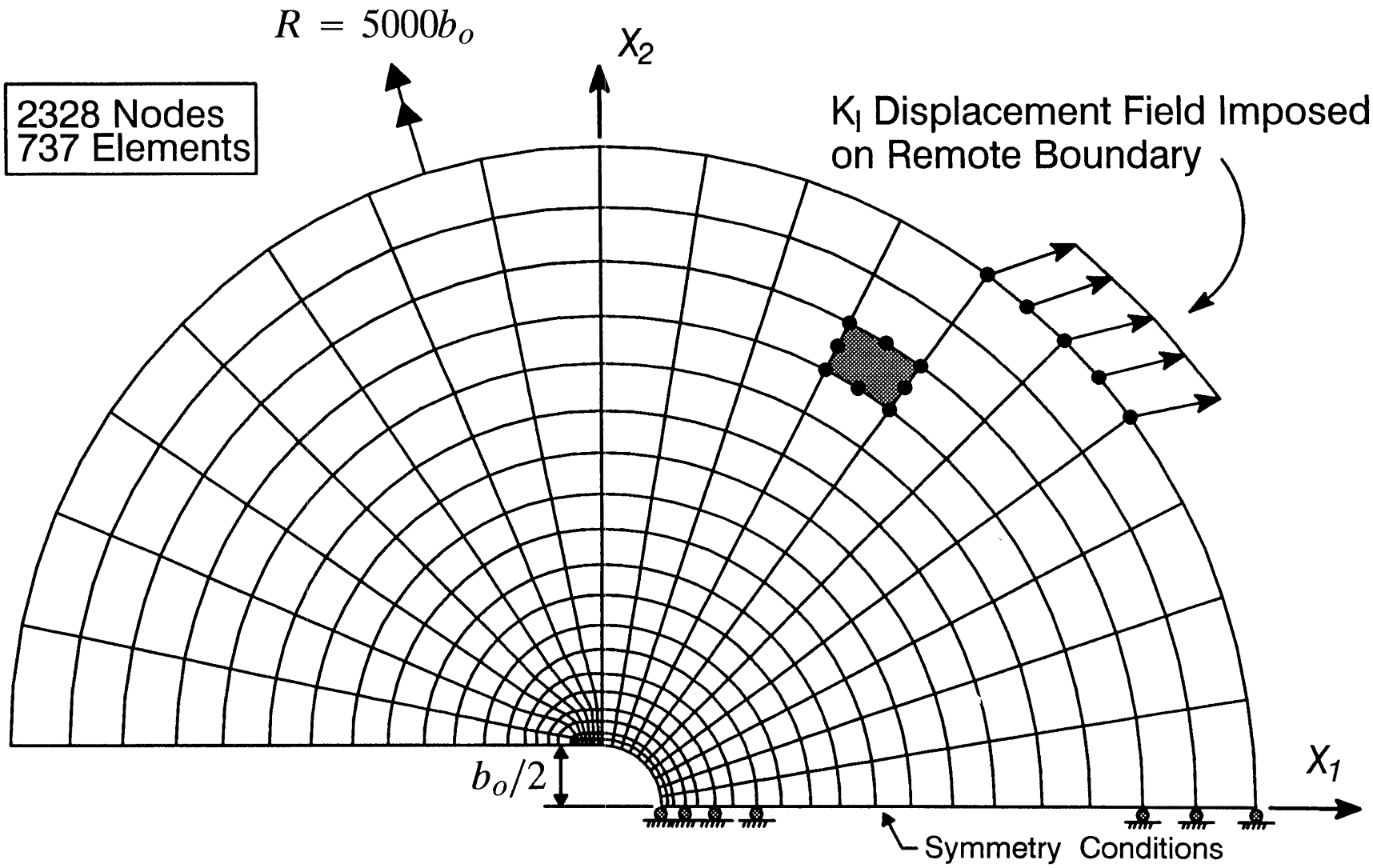

Fig. 4. Finite-element model (plane-strain) for boundary layer idealization of the small-scale yielding problem.

Figure 5 shows the deformed near–tip region at increasing levels of the notch opening. Equivalent plastic strains in the notch–tip element exceed 2 at the maximum load. Figure 6 shows the opening mode Cauchy stress, $\sigma_{\theta\theta}$, and equivalent plastic strain ahead of the notch tip on the crack plane. The radial distance is normalized by J/σ_o where J is the value of Rice's J–integral [24]. A domain integral method [28] is used to extract J from the numerical solution; for SSY conditions $J = K_I^2(1-\nu^2)/E$. The notch opening b can be estimated as $0.5J/\sigma_o$; the horizontal axis thus spans $0 \rightarrow 10b$. Outside the 'blunting' zone of size $r \approx 3b$, the present stresses achieve a steady–state condition which scales with J/σ_o. Once $b/b_o > 3$, excellent agreement is observed between the present stresses and those of a conventional small–strain model containing a sharp crack tip (modeled by singularity elements). The plastic strain distribution, shown for maximum load in Fig. 6, reveals that the zone of finite strains extends to $r \approx 3b$ beyond which the strains are a only a few multiples of the yield strain ϵ_o. The small–strain, asymptotic stresses (HRR) of Hutchinson [13] and Rice and Rosengren [25] are shown for comparison. The present finite strain results for an initially blunt notch and those for a small–strain model with an initially sharp notch both fall below the HRR solution at increasing distances from the tip, i.e., the HRR solution contains only the leading term of the full SSY field and is correct only for $r \rightarrow 0$.

Each of the 40 loading increments required an average of 3 iterations for convergence. Elements at the notch–tip sustain strain increments of about 4.3% or $21 \times \epsilon_o$. To gauge the convergence rate, this problem was analyzed using a conventional small–strain plasticity model—the same number of iterations were required for convergence. The finite–strain solution required 10% more CPU time than the corresponding small–strain analysis. A solution using 200 increments produced essentially no difference in the stresses and a maximum 1.5% difference in notch–tip strains. A solution with 20 increments converged without difficulty but with a loss of accuracy in notch–tip strains.

6. SUMMARY AND CONCLUSIONS

The numerical implementation of a flow theory plasticity model suitable for large strains and large rotations has been presented. The constitutive computations are formulated using strains, stresses, and their rates cast on the *unrotated* reference frame thereby removing many of the complicating details of previous finite strain models. Polar decomposition of the deformation gradients is employed to establish the unrotated reference frame; the resulting constitutive model is equivalent to one based on the Green–Naghdi stress rate but much simpler to implement numerically. The stress updating process is developed for an implicit, Total Lagrangian formulation of the finite–element method. Details of the various transformations and the consistent tangent modulus are given including a very efficient algorithm for 3–D polar decomposition. This finite–strain material model retains

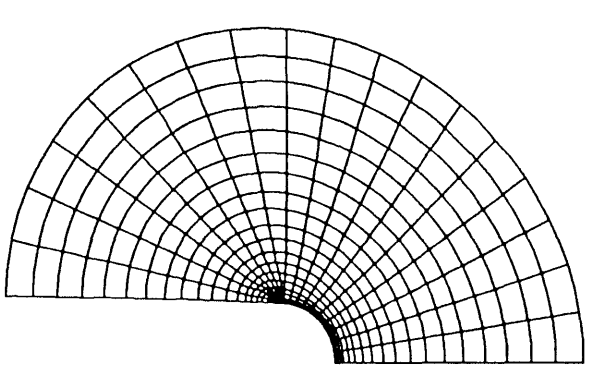

(a)

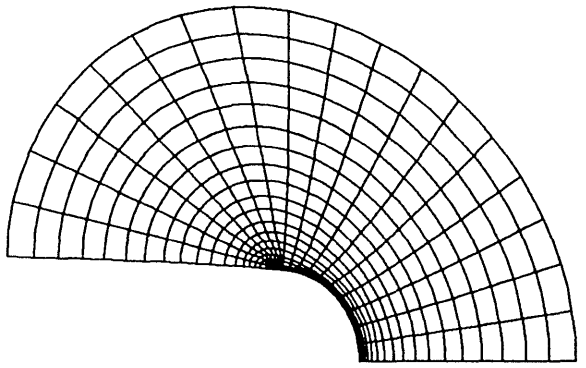

(b)

Note: Deformations to Scale

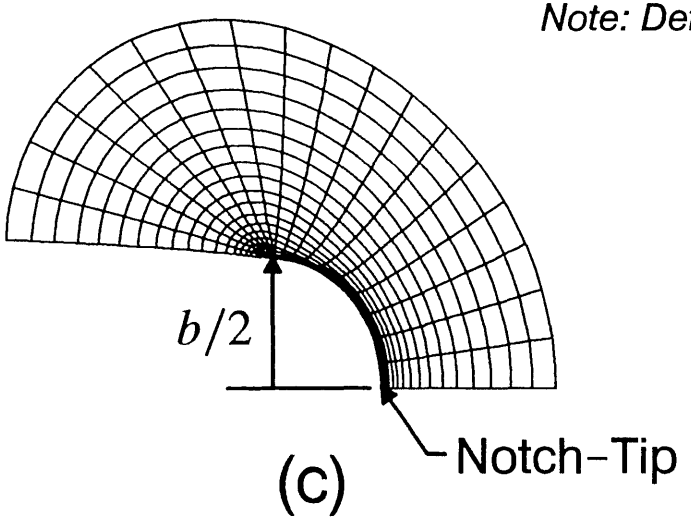

(c)

	b/b_o	ϵ_{pl} @ Notch–Tip
(a)	2.13	1.00
(b)	3.36	1.58
(c)	4.96	2.08

Fig. 5. Crack–tip deformations for increasing applied load in the SSY model.

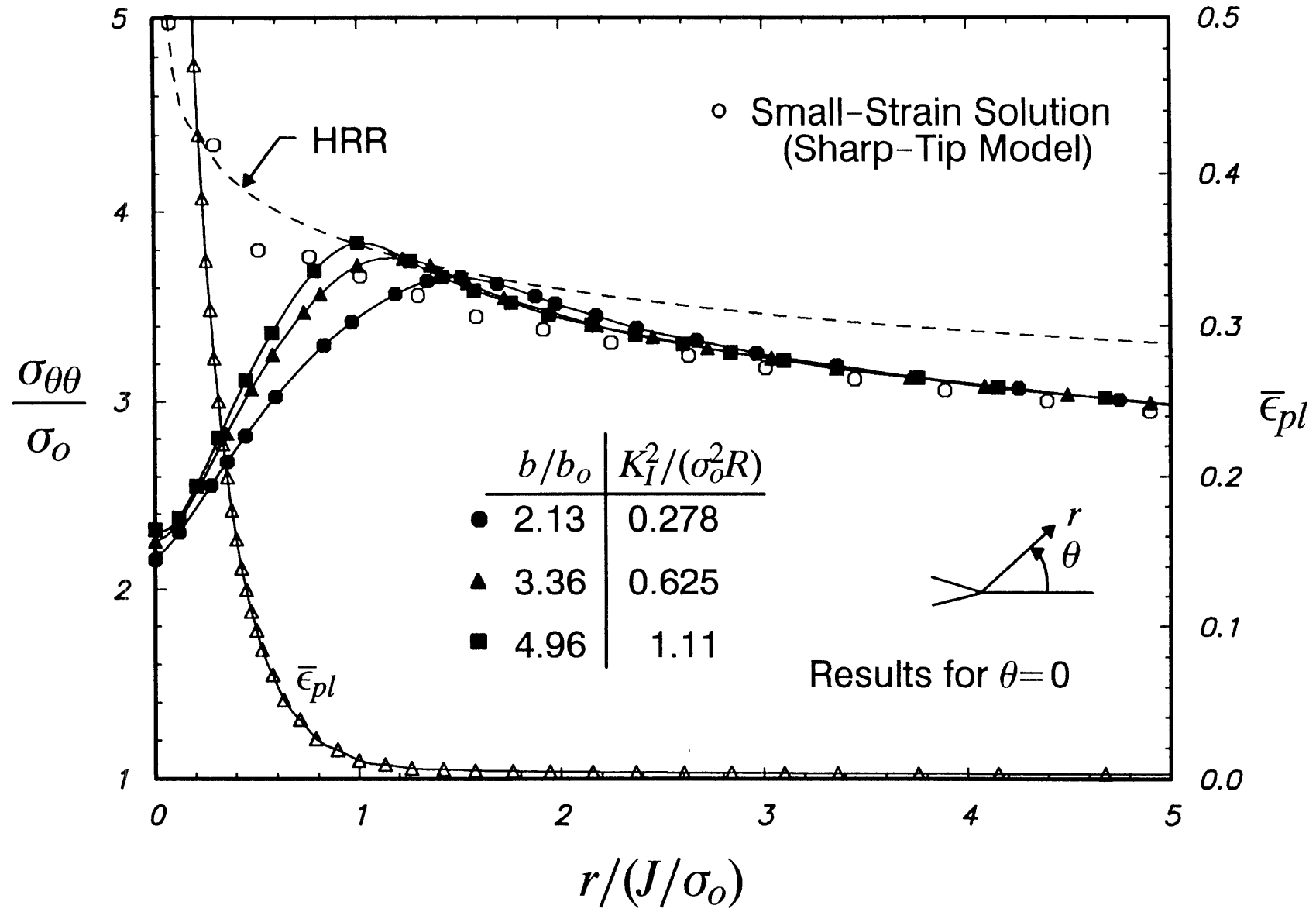

Fig. 6 Comparison of finite-element results for initially blunt tip with asymptotic HRR fields and with sharp-tip models (r and θ are coordinates in initial configuration).

the full numerical architecture of a conventional small–strain plasticity model with isotopic–kinematic hardening and has been implemented as a pre– and post– processor for such a model in our finite–element code.

Numerical tests demonstrate that for an implicit global solution, the computational effort required for the polar decompositions is insignificant relative to the effort required for updating element stiffnesses. Three numerical examples illustrate the acceptable responses predicted by the material model for simple homogeneous deformation of an incremental, linear–elastic material and for ductile fracture analyses of a material following incremental plasticity. Large step sizes are accommodated without undue loss of solution accuracy or convergence rate of the global equilibrium iterations.

7. REFERENCES

1. *ABAQUS* User's Manual, Version 4.8, Hibbitt, Karlsson & Sorensen, Inc., Providence R.I., 1990.

2. Atluri, S. N.,"On constitutive relations at finite strain: hypo–elasticity and elasto–plasticity with isotropic and kinematic hardening," *Computer Methods in Applied Mechanics and Engineering*, Vol. 43, 1984, pp. 137–171.

3. Asaro, R. J., "Crystal Plasticity," *Journal of Applied Mechanics,* 50, 1984, pp. 1–12.

4. Bathe, K. J., "Finite element procedures in engineering analysis," Prentice–Hall, 1982.

5. Dienes, J. K., "On the analysis of rotation and stress rate in deforming bodies," *Acta Mechanica*, Vol. 32, 1979, pp. 217–232.

6. Dodds, R. H., and Lopez, L. A., "Software virtual machines for development of finite–element systems," *International J. for Engineering with Computers,* Vol. 13, 1985, pp. 18–26.

7. Dodds, R. H., "Numerical techniques for plasticity computations in finite–element analysis," *Computers & Structures*, Vol. 26, No. 5, 1987, pp. 767–779.

8. Flanagan, D. P., and Taylor, L. M., "An accurate numerical algorithm for stress integration with finite rotations," *Computer Methods in Applied Mechanics and Engineering*, Vol. 62, 1987, pp. 305-320.

9. Green, A. E., and Naghdi, P. M., "A general theory of an elastic–plastic continuum," *Arch. Rat. Mech. Anal.*, Vol. 18, No. 1965, pp. 251.

10. Hibbitt, H. D., Marcal, P. V., and Rice, J. R., "A finite element formulation for problems of large strain and displacement," *International Journal of Solids and Structures,* Vol. 6, 1970, pp 1069–1086.

11. Hoger, A., and Carlson, D. E.,"Determination of the stretch and rotation in the polar decomposition of the deformation gradient," *Quarterly of Applied Mathematics*, Vol. 10, 1984.

12. Hughes, T. J. and Winget, J., "Finite rotation effects in numerical integration of rate constitutive equations arising in large-deformation analysis," *International J. for Numerical Methods in Engineering,* Vol. 15 (12), 1980, pp. 1862-1867.

13. Hutchinson, J. W., "Singular behavior at the end of a tensile crack in a hardening material," *Journal of the Mechanics and Physics of Solids, Vol. 16,* 1968, pp. 13-31.

14. Jaumann, G., "Geschlossenes system physikalischer und chemisher differentialgesefze," *Sitz Zer. Akad. Wiss. Wein, (IIa),* Vol. 120, 1911, pp. 385.

15. Johnson, G. C. and Bammann, D. J., "A discussion of stress rates in finite deformation problems," *International J. for Solids and Structures,* Vol. 20 (8), 1984, pp. 725-737.

16. Keppel, M. and Dodds, R. H., " Improved numerical techniques for plasticity computations in finite-element analysis," *Computers & Structures,* Vol. 36, No. 1, 1990, pp. 183-185.

17. Key, S. W. and Krieg, R. D., "On the numerical implementation of inelastic time dependent and time independent, finite strain constitutive equations in structural mechanics," *Computer Methods in Applied Mechanics and Engineering,* Vol. 33, 1982, pp. 439-452.

18. Kojic, M., and Bathe, K. J., "Studies of finite-element procedures: stress solution of a closed elastic strain path with stretching and shearing using the Updated Lagrangian Jaumann formulation," *Computer and Structures,* Vol. 26, No. 1/2, 1987, pp. 175-179.

19. Krieg, R. D., and Key, S. W. "Implementation of a time independent plasticity theory into structural computer programs. In *Constitutive Equations in Viscoplasticity: Computational and Engineering Aspects, AMD-20* (Edited by J. A. Stricklin and K. J. Saczalski), ASME, New York, 1976, pp. 125-138.

20. McMeeking, R. M., and Rice, J. R., "Finite-element formulations for problems of large elastic-plastic deformation," *International Journal of Solids and Structures,* Vol. 11, 1975, pp 601-616.

21. McMeeking, R. M., "Finite deformation analysis of crack-tip opening in elastic-plastic materials and implications for fracture," *Journal of the Mechanics and Physics of Solids, Vol. 25,* 1977, pp. 357-381.

22. Nagtegaal, J. C., and de Jong, J. E., "Some computational aspects of elastic-plastic, large strain analysis," *International J. for Numerical Methods in Engineering,* Vol. 12, 1981, pp. 15-41.

23. Pinsky, P. M., Ortiz, M., and Pister, K. S., "Numerical integration of rate constitutive equations in finite deformation analysis," *Computer Methods in Applied Mechanics and Engineering,* Vol. 40, 1983, pp. 137-158.

24. Rice, J. R.,"A path independent integral and the approximate analysis of strain concentrations by notches and cracks," *Journal of Applied Mechanics, Vol. 35,* 1968, pp. 379-386.

25. Rice, J. R., and Rosengren, G. F., "Plane strain deformation near a crack tip in a power law hardening material," *Journal of the Mechanics and Physics of Solids, Vol. 16,* 1968, pp. 1-12.

26. Rice, J. R., and Tracey, D. M., "Computational fracture mechanics," in *Numerical and Computer Methods in Structural Mechanics,* eds. S.J. Fenves, et al., Academic Press, New York, 1968, pp. 585-623.

27. Roy, S., Fossum, A. F., and Dexter, R. J., "On the use of polar decomposition in the integration of hypo–elastic constitutive laws," submitted for publication.

28. Shih, C. F., Moran, B., and Nakamura, T., "Energy release rate along a three–dimensional crack front in a thermally stressed body," *International J. of Fracture,* Vol. 30, 1986, pp. 79–102.

29. Simo, J. C., and Ortiz, M., "A unified approach to finite deformation elasto–plastic analysis based on the use of hyper–elastic constitutive equations," *Computer Methods in Applied Mechanics and Engineering,* Vol. 49, 1985, pp. 221–245.

30. Simo, J. C., and Taylor, R. S., "Consistent tangent operators for rate–independent elasto–plasticity," *Computer Methods in Applied Mechanics and Engineering,* Vol. 48, 1985, pp. 101–118.

31. Simo, J. C., and Taylor, R. S., "A return mapping algorithm for plane stress elasto–plasticity," *International J. of Numerical Methods in Engineering,* Vol. 22, 1986, pp. 649–670.

32. Taylor, L. M. and Flanagan, D. P., "PRONTO 2D, a two–dimensional transient solid dynamics program," *SAND86–0594,* Sandia National Laboratories, Albuquerque, NM, 1987.

APPENDIX A

FORTRAN CODE FOR POLAR DECOMPOSITION

```
c ***************************************************
c *                                                 *
c *   mtmplr -- polar decomposition of the deformation *
c *             gradient into the rotation tensor and  *
c *             the right stretch tensor. (3x3)        *
c *                                                 *
c ***************************************************
c
c
      subroutine mtmplr( f, r, u, ui, detf )
      implicit integer (a-z)
      real  f(3,3), r(3,3), u(6), ui(6), c(6), cc(6),
     &      ev(3), ct(6), iu, iiu, iiiu, a1, b1, c1, a2,
     &      b2, c2, d2, detf
c
c             c,cc,u and ui are in symmetric
c             upper triangular form.
c
c             compute the metric tensor.
c
      c(1) = f(1,1)*f(1,1)+f(2,1)*f(2,1)+f(3,1)*f(3,1)
      c(2) = f(1,1)*f(1,2)+f(2,1)*f(2,2)+f(3,1)*f(3,2)
      c(3) = f(1,2)*f(1,2)+f(2,2)*f(2,2)+f(3,2)*f(3,2)
      c(4) = f(1,1)*f(1,3)+f(2,1)*f(2,3)+f(3,1)*f(3,3)
      c(5) = f(1,2)*f(1,3)+f(2,2)*f(2,3)+f(3,2)*f(3,3)
      c(6) = f(1,3)*f(1,3)+f(2,3)*f(2,3)+f(3,3)*f(3,3)
c
      ct(1) = c(1)
      ct(2) = c(3)
      ct(3) = c(6)
      ct(4) = c(2)
      ct(5) = c(5)
      ct(6) = c(4)
c
c             compute the square of the metric tensor.
c
      cc(1) = c(1)*c(1)+c(2)*c(2)+c(4)*c(4)
      cc(2) = c(1)*c(2)+c(2)*c(3)+c(4)*c(5)
      cc(3) = c(2)*c(2)+c(3)*c(3)+c(5)*c(5)
      cc(4) = c(1)*c(4)+c(2)*c(5)+c(4)*c(6)
      cc(5) = c(2)*c(4)+c(3)*c(5)+c(5)*c(6)
      cc(6) = c(4)*c(4)+c(5)*c(5)+c(6)*c(6)
c
c             compute the principal values of the
c             metric tensor.
c
      call mtmevd( ct, ev )
c
c             compute the invariants of the right
c             stretch tensor. the determinant of
c             deformation tensor is product of
c             right stretch eigenvalues.
c
      ev(1) = sqrt(ev(1))
      ev(2) = sqrt(ev(2))
      ev(3) = sqrt(ev(3))
c
      iu    = ev(1)+ev(2)+ev(3)
      iiu   = ev(1)*ev(2)+ev(2)*ev(3)+ev(1)*ev(3)
      iiiu  = ev(1)*ev(2)*ev(3)
      detf  = iiiu
c
c             compute the right stretch tensor.
c
      a1 = 1.0/(iu*iiu-iiiu)
      b1 = iu*iiiu
      c1 = iu*iu-iiu
c
      u(1) = a1 * ( b1 + c1*c(1) - cc(1) )
      u(2) = a1 * (      c1*c(2) - cc(2) )
      u(3) = a1 * ( b1 + c1*c(3) - cc(3) )
      u(4) = a1 * (      c1*c(4) - cc(4) )
      u(5) = a1 * (      c1*c(5) - cc(5) )
      u(6) = a1 * ( b1 + c1*c(6) - cc(6) )
c
c             compute the inverse of the right
c             stretch tensor.
c
      a2 = 1.0/(iiiu*(iu*iiu-iiiu))
      b2 = iu*iiu*iiu-iiiu*(iu*iu+iiu)
      c2 = -iiiu-iu*(iu*iu-2.0*iiu)
      d2 = iu
c
      ui(1) = a2 * ( b2 + c2*c(1) + d2*cc(1) )
      ui(2) = a2 * (      c2*c(2) + d2*cc(2) )
      ui(3) = a2 * ( b2 + c2*c(3) + d2*cc(3) )
      ui(4) = a2 * (      c2*c(4) + d2*cc(4) )
      ui(5) = a2 * (      c2*c(5) + d2*cc(5) )
      ui(6) = a2 * ( b2 + c2*c(6) + d2*cc(6) )
c
c             compute the rotation tensor.
c
      r(1,1) = f(1,1)*ui(1)+f(1,2)*ui(2)+f(1,3)*ui(4)
      r(1,2) = f(1,1)*ui(2)+f(1,2)*ui(3)+f(1,3)*ui(5)
      r(1,3) = f(1,1)*ui(4)+f(1,2)*ui(5)+f(1,3)*ui(6)
      r(2,1) = f(2,1)*ui(1)+f(2,2)*ui(2)+f(2,3)*ui(4)
      r(2,2) = f(2,1)*ui(2)+f(2,2)*ui(3)+f(2,3)*ui(5)
      r(2,3) = f(2,1)*ui(4)+f(2,2)*ui(5)+f(2,3)*ui(6)
      r(3,1) = f(3,1)*ui(1)+f(3,2)*ui(2)+f(3,3)*ui(4)
      r(3,2) = f(3,1)*ui(2)+f(3,2)*ui(3)+f(3,3)*ui(5)
      r(3,3) = f(3,1)*ui(4)+f(3,2)*ui(5)+f(3,3)*ui(6)
c
      return
      end
c ***************************************************
c *                                                 *
c *   mtmevd -- compute eigenvalues of 3x3 symmetric *
c *             matrix stored in packed format      *
c *                                                 *
c ***************************************************
```

```
c
c
      subroutine mtmevd( k, lamda )
      implicit integer (a-z)
      real   k(1),lamda(1),kbari,kbarj,kbar,ki,
     &       kj,mi,mj,scale,alpha,gamma,x,xsign,jactol,
     &       thold,sqtol,ratiok,rad,errork,swap,
     &       m1,m2,m3,k1,k2,k3,k4,k5,k6
      logical cvgtst
      data maxswp/15/,jactol/1.0e-04/
c
c             initialize lamda, m, sweep parameters.
c
      m1 = 1.0
      m2 = 1.0
      m3 = 1.0
      k1 = k(1)
      k2 = k(2)
      k3 = k(3)
     .k4 = k(4)
      k5 = k(5)
      k6 = k(6)
      lamda(1) = k1
      lamda(2) = k2
      lamda(3) = k3
      swpnum   = 0
c
c             scale [k] to avoid potential problems
c             with exponential overflow and underflow.
c
      kj = k1
      kj = min( k2,kj )
      kj = min( k3,kj )
      ki = k1
      ki = max( k2,ki )
      ki = max( k3,ki )
      mj = 1.0
      mi = 1.0
c
c             compute the scale factor and do the scaling
c
      iexp  = int( ( log10(kj)+log10(ki) ) * 0.25 )
      scale = 1.0 / ( 10.0 ** iexp )
      m1 = m1 * scale
      m2 = m2 * scale
      m3 = m3 * scale
      k1 = k1 * scale
      k4 = k4 * scale
      k2 = k2 * scale
      k6 = k6 * scale
      k5 = k5 * scale
      k3 = k3 * scale
c
c             begin a new sweep
c
   10 swpnum = swpnum + 1
      thold  = 0.0001 ** swpnum
      sqtol  = jactol * jactol
      if ( thold .lt. sqtol ) thold = sqtol
c
c             enter sweep loop -- work on lower triangle
c             only. rows are done from top to bottom
c             columns are done from left to right.
c             skip when already within tolerance.
c
      ratiok = ( k4*k4)  / ( k2*k1 )
      if ( ratiok .lt. thold ) go to 15
      kbari = -m2 * k4
      kbarj = -m1 * k4
      kbar  =  k2 * m1 - k1 * m2
      rad   = ( kbar * kbar / 4.0 ) + kbari * kbarj
      xsign = 1.0
      x     = kbar / 2.0 + sign(xsign, kbar) * sqrt(rad)
      if ( (abs(x).lt.jactol*abs(kbarj)) .or.
     &     (abs(x).lt.jactol*abs(kbari)) ) then
         alpha = 0.0
         gamma = -k4 / k2
      else
         alpha =  kbarj / x
         gamma = -kbari / x
      end if
      ki = k5
      kj = k6
      k5 = ki + gamma * kj
      k6 = kj + alpha * ki
      kj = k1
      mj = m1
      ki = k2
      mi = m2
      k1 = kj + alpha * alpha * ki + 2.0 * alpha * k4
      m1 = mj + alpha * alpha * mi
      k2 = ki + gamma * gamma * kj + 2.0 * gamma * k4
      m2 = mi + gamma * gamma * mj
      k4 = 0.0
c
c             row 3 and column 1
c             ------------------
c
   15 ratiok = ( k6*k6 ) / ( k3*k1 )
      if ( ratiok .lt. thold ) go to 20
      kbari = -m3 * k6
      kbarj = -m1 * k6
      kbar  =  k3 * m1 - k1 * m3
      rad   =  ( kbar * kbar / 4.0 ) + kbari * kbarj
      xsign =  1.0
      x     =  kbar / 2.0 + sign(xsign, kbar) * sqrt(rad)
      if ( (abs(x).lt.jactol*abs(kbarj)) .or.
     &     (abs(x).lt.jactol*abs(kbari)) ) then
         alpha = 0.0
```

```
         gamma = -k6 / k3
      else
         alpha =  kbarj / x
         gamma = -kbari / x
      end if
      ki = k5
      kj = k4
      k5 = ki + gamma * kj
      k4 = kj + alpha * ki
      kj = k1
      mj = m1
      ki = k3
      mi = m3
      k1 = kj + alpha * alpha * ki + 2.0 * alpha * k6
      m1 = mj + alpha * alpha * mi
      k3 = ki + gamma * gamma * kj + 2.0 * gamma * k6
      m3 = mi + gamma * gamma * mj
      k6 = 0.0
c
c             row 3 and column 2
c             ------------------
c
 20   ratiok = ( k5*k5 ) / ( k3*k2 )
      if ( ratiok .lt. thold ) go to 25
      kbari = -m3 * k5
      kbarj = -m2 * k5
      kbar  =  k3 * m2 - k2 * m3
      rad   =  ( kbar * kbar / 4.0 ) + kbari * kbarj
      xsign =  1.0
      x     =  kbar / 2.0 + sign(xsign, kbar) * sqrt(rad)
      if ( (abs(x).lt.jactol*abs(kbarj)) .or.
     &     (abs(x).lt.jactol*abs(kbari)) ) then
         alpha = 0.0
         gamma = -k5 / k3
      else
         alpha =  kbarj / x
         gamma = -kbari / x
      end if
      ki = k6
      kj = k4
      k6 = ki + gamma * kj
      k4 = kj + alpha * ki
      kj = k2
      mj = m2
      ki = k3
      mi = m3
      k2 = kj + alpha * alpha * ki + 2.0 * alpha * k5
      m2 = mj + alpha * alpha * mi
      k3 = ki + gamma * gamma * kj + 2.0 * gamma * k5
      m3 = mi + gamma * gamma * mj
      k5 = 0.0
c
c             end of sweep loop
c             -----------------
c
c             update eigenvalue vector -- lamda
c
 25   lamda(1) = k1 / m1
      lamda(2) = k2 / m2
      lamda(3) = k3 / m3
c
c             check off-diagonal elements for convergence
c             -------------------------------------------
c
      cvgtst = .true.
c
      errork = k4 * k4 / ( k2 * k1 )
      if ( errork .gt. sqtol ) cvgtst = .false.
c
      errork = k6 * k6 / ( k3 * k1 )
      if ( errork .gt. sqtol ) cvgtst = .false.
c
      errork = k5 * k5 / ( k3 * k2 )
      if ( errork .gt. sqtol ) cvgtst = .false.
c
      if ( cvgtst ) go to 30
      if ( swpnum .lt. maxswp ) go to 10
c
c             eigenvalues have converged. reorder and exit.
c
 30   if ( lamda(2) .lt.lamda(1) ) then
         swap     = lamda(1)
         lamda(1) = lamda(2)
         lamda(2) = swap
      end if
c
      if ( lamda(3) .lt. lamda(1) ) then
         swap     = lamda(1)
         lamda(1) = lamda(3)
         lamda(3) = swap
      end if
c
      if ( lamda(3) .lt. lamda(2) ) then
         swap     = lamda(2)
         lamda(2) = lamda(3)
         lamda(3) = swap
      end if
c
c
      return
      end
```